RIS-enabled mmWave Channel Sounding Based on Electronically Reconfigurable Transmitarrays

Alfred Mudonhi*†‡, Marina Lotti*†, Antonio Clemente*†, Raffaele D'Errico*†, Claude Oestges‡
*CEA-Leti, Grenoble, France, alfred.mudonhi@cea.fr, marina.lotti@cea.fr, antonio.clemente@cea.fr, raffaele.derrico@cea.fr
†Université Grenoble-Alpes, Grenoble, France
‡ICTEAM-Universite catholique de Louvain, Belgium, claude.oestges@uclouvain.be

***Abstract*—In this paper we present a millimeter wave radio channel sounding campaign, enabled by Reconfigurable Intelligent Surfaces (RISs). The measurement setup is based on an electronically reconfigurable Transmitting-RIS (T-RIS) composed by 400 unit-cells. Optimal phase distributions were implemented in order to operate a beam scan over 120 degrees. Two indoor scenarios were investigated in the Ka Band, exploiting the beam scanning capabilities of the antenna. The results in terms of path loss and delay spread are presented and discussed.**

***Index Terms*—Indoor channel, millimiter waves, Reconfigurable Intelligent Surfaces, Transmitarray.**

I. INTRODUCTION

Massive multiple-input multiple-output (MIMO) technology involves the deployment of numerous antennas, generally at the base station, in order to increase channel capacity, link reliability, and eventually provide enhanced security [1]. Literature has been focusing on sub$-$6 GHz massive MIMO channels, showing the benefits of these approaches [2], [3], [4], [5].

In the development of 5G and beyond networks, millimeter waves technologies are expected to play a main role to attain unpreceded performance of low-latency and high-date rate. These technologies are often considered in combination with massive MIMO transmission and beamforming antennas to counteract the poor link budgets [6]. Reconfigurable Intelligent Surfaces (RIS) are nowadays considered as a new paradigm for wireless communictation [7]. The interaction with electric and/or magnetic fields, is typically provided by resonant effects controlled by the geometry of the unit cells and their distribution, enabling antenna performance enhancement (beamshaping), flat lens, artificial magnetic conductors, cloaking, absorbers and scattering reduction. Indeed, one of the use of these surfaces is to realize reflect- or transmitarrays as solutions for applications requiring high gain and efficiency, and wide field of view (>60°) scanning capabilities. These technologies have recently emerged as a promising alternative to the traditional phased arrays. In the past fixed beam transmitarrays have already been used for channel characterization in the V-band for backscattering measurements [8].

In this paper we present a transmitting RIS-based mmwave channel sounder setup enabled by a electronically reconfigurable transmitarray. With respect of the state of the art, electronic steering of the beam is obtained through phase distribution on 400 unit cells. The rest of the paper is structured as follows: in Section II, the measurement setup and characteristics of the electronically reconfigurable transmit array are presented. Section III discusses the results of the considered scenarios and Section IV concludes the paper.

II. RIS-ENABLED CHANNEL SOUNDING SETUP

A. Electronically Reconfigurable Transmitarray

The Transmitting-RIS (T-RIS) here considered is an electronically reconfigurable transmitarray composed of 400-elements (or unit-cells), which are positioned in a 20×20 square aperture of size 10.2×10.2 cm^2 [9], as shown in Fig. 1. It is based on linearly polarized 1-bit unit-cells with 180° phase-shifting capability. They permit the generation of both right hand (RH) or left hand (LH) circular polarizations depending on the phase distribution, despite a 3dB lower gain in comparison with an array composed of circularly-polarized unit-cells. In order to obtain circular polarization from the linearly polarized unit-cells, a sequential rotation is usually applied to the transmitting layer. In the particular T-RIS we used, the active unit-cell side loaded by p-i-n diodes is placed on the receiving layer and the rotation is applied to the transmitting layer (i.e passive unit-cell side). In order to improve the tilting capabilities of the T-RIS, and prevent the appearance of grating lobes on diagonal planes, a *random* sequential rotation scheme is applied to the transmitting layer of the T-RIS. For more details about the designing of the transmitarray, refer to [9].

The phase compensation, i.e. the phase shift provided by each unit-cell through a proper bias of the p-i-n diodes, is computed using an optimization tool. The combination of the receiving layer, the phase compensation and the rotation scheme of the patch elements on the transmitting layer gives the wanted phase distribution on the radiating aperture. In this architecture a 1-bit phase control is implemented, therefore it is possible to choose the phase of either 0° or 180° through two diodes. The T-RIS prototype and architecture are shown in Fig. 1.

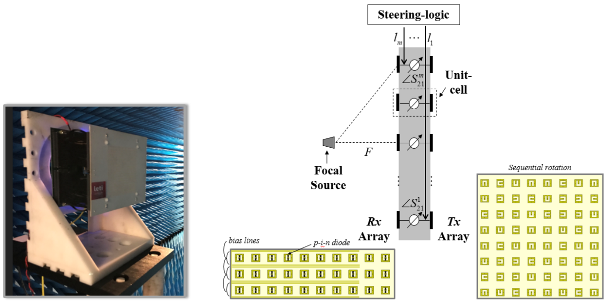

(a) (b)

Fig. 1. Transmitting-RIS [9]: protoype (a), architecture (b).

By changing the phase distribution, on the RIS we can electronically reconfigure the radiation pattern and realize beamsteering. The result of the phase distribution and corresponding gain pattern is shown in Fig. 2, for the steering angle of $\phi_s = 0°$ and $\phi_s = 30°$.

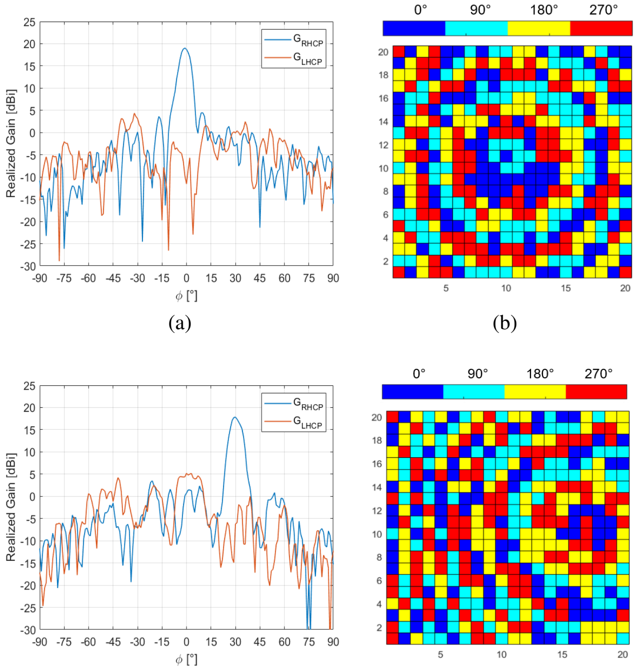

(a) (b)

(c) (d)

Fig. 2. Gain pattern (a),(c) and phase distribution (b),(d) for $\phi_s = 0°$ and $\phi_s = 30°$.

Once the phase distribution has been optimized, the T-RIS vector transfer function can be written as:

$$\mathbf{H}(f, \theta, \phi, \theta_s, \phi_s) = H_v(f, \theta, \phi, \theta_s, \phi_s)\widehat{a_v} \pm jH_h(f, \theta, \phi, \theta_s, \phi_s)\widehat{a_h} \tag{1}$$

where $H_v(f, \theta, \phi, \theta_s, \phi_s)$ is the vertical component and $H_h(f, \theta, \phi, \theta_s, \phi_s)$ is the horizontal component, θ, ϕ are the pattern elevation and azimuthal angles respectively, θ_s, ϕ_s are the elevation and azimuthal steering angles, respectively. The measured gain patterns for circular polarization at 28 GHz, considering different steering angles, are shown in Fig. 3(a). The maximum gain for $\phi_s = 0°$ is 15.9 dBi and 18.7 dBic, respectively, while for a maximum steering angle of $-60°$ the gain drops to 7.87 dBi and 11.94 dBic, respectively. The steering angle varies as a function of frequency, due to the beam squint, but the effect remains limited even for larger pointing angles, as shown in Fig. 3(b), where the beam squint for the steering angle $\phi_s = 30°$ is reported.

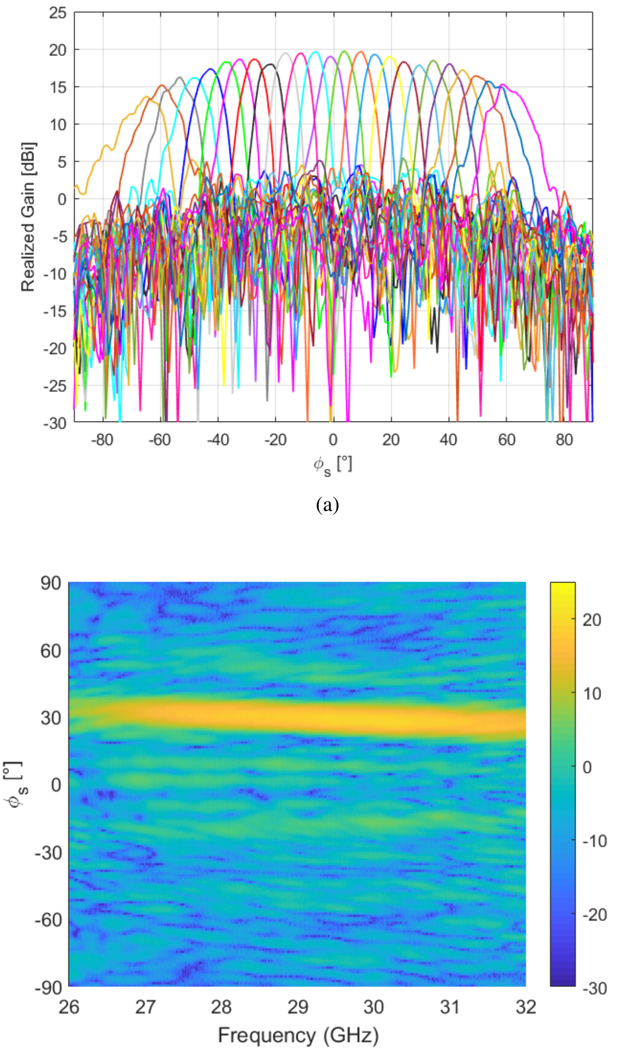

(a)

(b)

Fig. 3. TA measured gain patterns for $+/-60°$ steering angles for right circular (a) polarization and (b) beam squint for $\phi_s = 30°$.

B. Channel Measurement Setup

In this section we present the RIS-enabled channel sounding setup . The measurement setup is shown in Fig. 4. An external PC controls the measurement instruments. The measurement setup consists of a four-ports Vector Network Analyzer operating in the frequency range 24-40 GHz; one T-RIS (size 20×20, 1 bit); one monopole antenna and an X-Y-Z positioner. A 4 GHz bandwidth was measured in the frequency band 26-30 GHz sweeping 801 frequency points. The transmitted power was 10 dBm. The receiver (rx) and the transmitter (tx) were both 1.52 m above the ground. On the transmitting side there is the T-RIS presented in the previous section while on the receiving side, a vertically polarized monopole antenna is considered. The monopole is placed on a x-y scanner to perform spatial grid of 3 $\times$ 3 by wavelength step. The monopole antenna is characterized by 0 dBi maximum gain in the vertical polarization. The T-RIS optimized gain in the broadside direction at 28 GHz was 18.7 dBic. The T-RIS scans the environment in the following fashion: ϕ_s varies from -60° to 60° following a step of 5°. This implies that at each particular receiver position, 25 beam scans are considered.

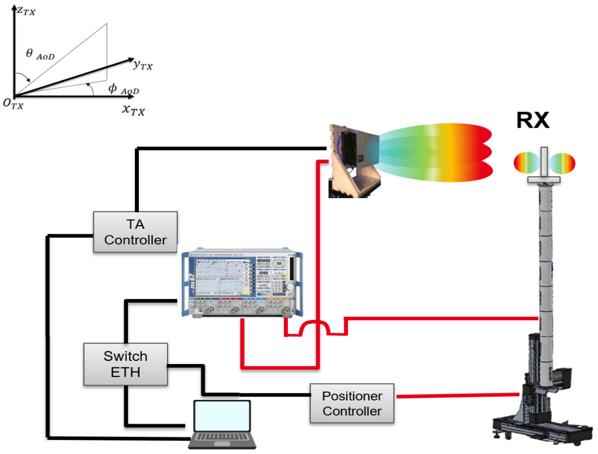

Fig. 4. RIS-enabled channel measurement setup.

III. Channel Measurement Campaign and Results

In this section, we present a measurement campaign in two indoor scenarios and discuss the channel characteristics obtained.

A. *Scenario 1*

The channel measurement campaign was conducted in a laboratory room. The dimensions of the room were 72.41 m^2. The laboratory room is furnished with tables, chairs, desktops, sofas, and a televison as clearly depicted in the figures, Fig. 5(a) and Fig. 5(b). The left walls of the room comprises mostly of glass windows and the right side walls also have a part with a glass window. On the roof, also present is a metalic positioner. Figure. 6 shows the power delay profile when $\phi_s = 0°$. A threshold of 10 dB above the noise floor was considered. For the aforementioned steering angle, the main beam is in the direction of receivers RX1, RX2, RX5 and RX6. As expected, the received power decreases with increase in transmitter-receiver separation distance. From figures, Fig. 7(a) and Fig. 7(b) showing the results for all the 8 receiver positions, we see that; as long as the receiver is in the main lobe direction, the overal path loss (antenna embedded) experienced is very low, thanks to the T-RIS directivity. For one tx-rx measured point (at each T-RIS steering angle), the overal path loss (antenna embedded), PL, is computed following equation (2). In particular, when the steering angle is $\phi_s = 0°$, we can see that the delay spread values and the overal path loss (antenna embedded) values of the receivers (RX1, RX2, RX5 and RX6) in the main beam direction have the least overal path loss (antenna embedded) and delay spreads values. For steering angles, $\phi_s = 15°$ and $\phi_s = -15°$, evidently, the receiver positions RX3 and RX4 which are in the main lobe direction record the least overal path loss (antenna embedded) and delay spread values, respectively. The same behaviour is evidenced for $\phi_s = 10°$ and $\phi_s = -10°$ whereby the least overal path loss (antenna embedded) and delay spread values are observed at receiver positions RX7 and RX8 respectively. We can clearly see from Fig. 7(b) that delay spreads values, as small as 6 ns are observed in the main lobe directions while values as high as 32 ns are observed in other directions. The values obtained are consistent with those found in the literature [10]. The small DS values in the main lobe direction are as a result of the narrow beam transmission which reduces the time dispersion [11]. Table I summarizes the expected and the measured angles of departure and LOS path powers respectively.

$$PL = \frac{1}{\sum_{n=1}^{N} |h(\tau_n)|^2} \tag{2}$$

where $h(\tau_n)$ is the channel impulse response obtained after the inverse Fourier transform operation on the measured channel transfer function (Hermitian or conjugate symmetry form), and N is the number of sweep points.

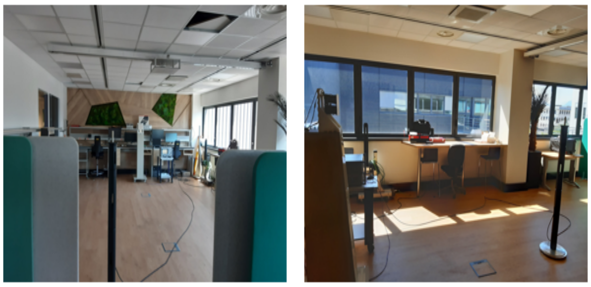

(a) Environment

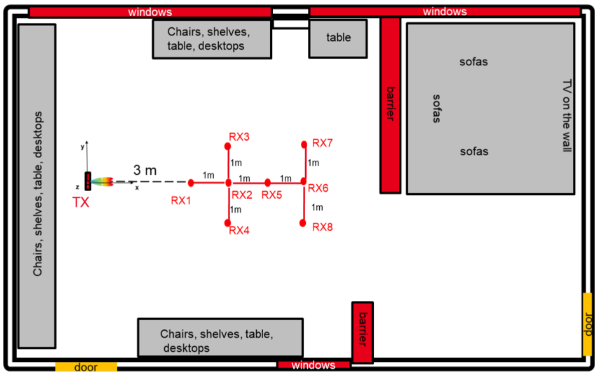

(b) Floor plans

Fig. 5. Measurement environment and floor plans for scenario 1.

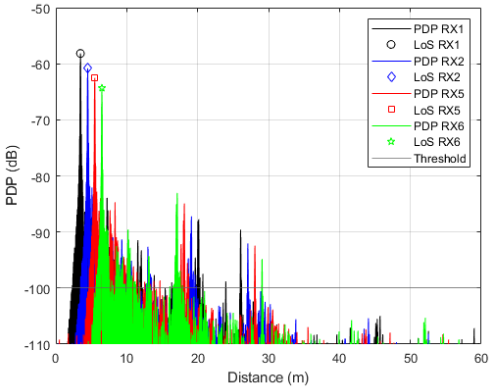

Fig. 6. PDPs for RX1, RX2, RX5 and RX6 at $\phi_s = 0°$.

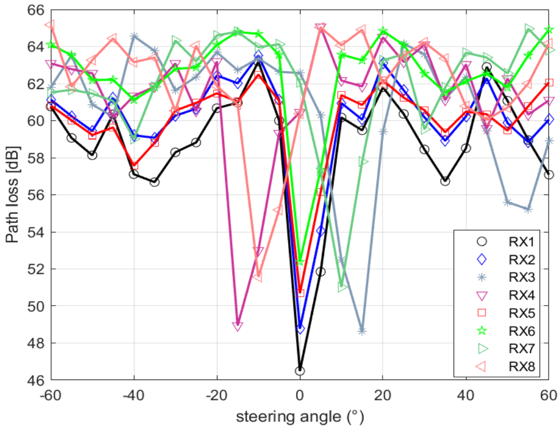

(a) Scenario 1 all receiver positions PL

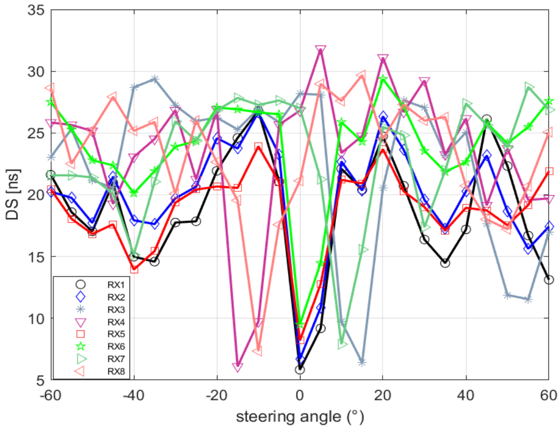

(b) Scenario 1 all receiver positions DS

Fig. 7. Overal path loss (antenna embedded) and delay spreads of scenario 1 for all receiver positions.

TABLE I
LOS PATH RESULTS.

Position	AOD (°)	ϕ_s(°)	Expected [dB]	Measured [dB]
RX1	0	0	-55	-58.3
RX2	0	0	-57.6	60.9
RX3	15	15	-57.8	-61.4
RX4	-15	-15	-57.8	-61.6
RX5	0	0	-59.5	-62.5
RX6	0	0	-61.1	-64.3
RX7	10	10	-61.2	-63.4
RX8	-10	-10	-61.2	-64.5

B. Scenario 2

The channel measurement campaign was conducted in an office room. The dimensions of the room were 28.54 m^2. The office room is virtually empty; it only has a storage unit shown in Fig. 8 (environment and floor plans). Here 3×3 spatial grids in the x and y axes are scanned at the receiver side.

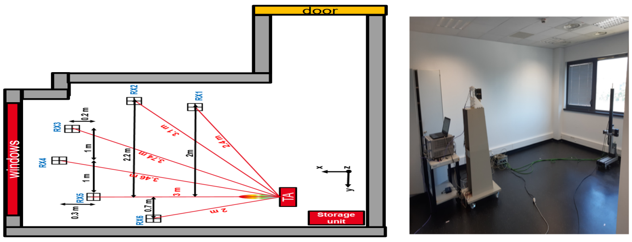

(a) Floor plans (b) Environment

Fig. 8. Measurement floor plans and environment for scenario 2.

This scenario, as shown in the floor plans, involves the T-RIS almost close to the right corner, where the storage unit is. With RX5 as the reference position, the strongest signal strength and the least delay spread values are obtained at $\phi_s = 0°$. The obtained results are consistent with the geometry of the room floor plans and significant reflections from the windows and the walls can be observed from the PDPs of the receivers. This is mainly because the receiver positions are very close to the windows and the walls as can be seen in the floor plans. Figures, Fig. 9(a) and Fig. 9(b) show the mean (overal path loss (antenna embedded) and DS) values per each steering angles, for all the considered receiver positions and the DS and PL values are least in the main beam directions for the same reasons already mentioned in scenario 1. Likewise, the overal path loss (antenna embedded), PL, for one tx-rx measured point (at each T-RIS steering angle), was computed following equation (2). Table II summarizes the expected and the measured angles of departure and LOS path powers respectively.

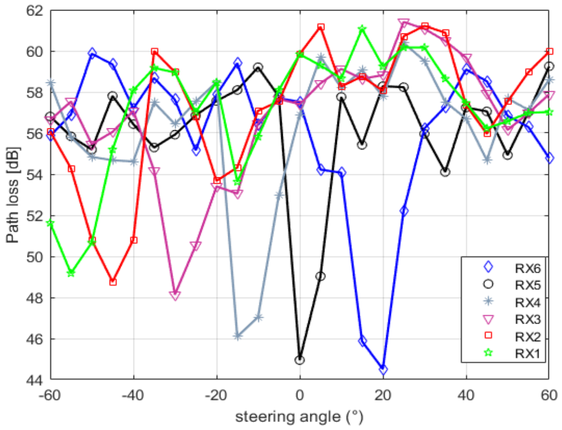

(a) Scenario 2 all receiver positions mean PL

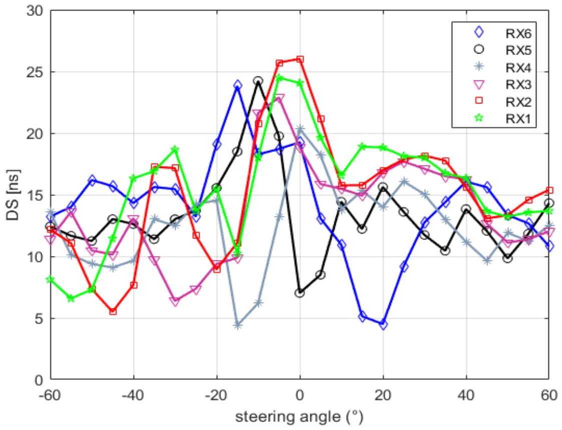

(b) Scenario 2 all receiver positions mean DS

Fig. 9. Overal mean path loss (antenna embedded) and delay spreads of scenario 2 for all receiver positions.

TABLE II
LOS PATH RESULTS.

Position	AOD(°)	ϕ_s(°)	Expected [dB]	Measured [dB]
RX1	-56	-55	-58.4	-61.3
RX2	-45	-45	-58.11	-60.9
RX3	-32	-30	-59.2	-60.6
RX4	-16.7	-15	-56.3	-57.9
RX5	0	0	-55	-56.8
RX6	21	20	-51.8	-56.1

IV. CONCLUSIONS

In this paper we exploited a Transmitting - Reconfigurable Intelligent Surface (T-RIS) for beamsteering channel sounding in mmwave. The setup is based on an electronically reconfigurable transmitarray of 400 elements, whose phase distribution is optimized to obtain beamsteering in circular and linear polarizations. The results show that antenna beamforming has a direct impact on both the delay spread (DS) and the path loss (PL) of the channel. When the T-RIS is steering towards the receivers in the main lobe direction, the DS is comprised between 5 and 10 ns, while larger values (up to 32 ns) were observed when steering in other directions. Likewise, the path losses in the main beam direction are reduced thanks to RIS beamforming capabilities, which leads to an improvement in the overall link budget.

ACKNOWLEDGMENT

This work was partially funded by the ANR projects MOREOVER and MESANGES, and H2020 project RISE-6G.

REFERENCES

[1] A. L. Swindlehurst, E. Ayanoglu, P. Heydari, and F. Capolino, “Millimeter-wave massive mimo: the next wireless revolution?” *IEEE Communications Magazine*, vol. 52, no. 9, pp. 56–62, 2014.

[2] E. G. Larsson, O. Edfors, F. Tufvesson, and T. L. Marzetta, “Massive mimo for next generation wireless systems,” *IEEE communications magazine*, vol. 52, no. 2, pp. 186–195, 2014.

[3] E. Björnson, J. Hoydis, and L. Sanguinetti, “Massive mimo networks: Spectral, energy, and hardware efficiency,” *Foundations and Trends in Signal Processing*, vol. 11, no. 3-4, pp. 154–655, 2017.

[4] L. Lu, G. Y. Li, A. L. Swindlehurst, A. Ashikhmin, and R. Zhang, “An overview of massive mimo: Benefits and challenges,” *IEEE journal of selected topics in signal processing*, vol. 8, no. 5, pp. 742–758, 2014.

[5] P. Zhang, J. Chen, X. Yang, N. Ma, and Z. Zhang, “Recent research on massive mimo propagation channels: A survey,” *IEEE Communications Magazine*, vol. 56, no. 12, pp. 22–29, 2018.

[6] J. Huang, C.-X. Wang, R. Feng, J. Sun, W. Zhang, and Y. Yang, “Multi-frequency mmwave massive mimo channel measurements and characterization for 5g wireless communication systems,” *IEEE Journal on Selected Areas in Communications*, vol. 35, no. 7, pp. 1591–1605, 2017.

[7] E. Basar, M. Di Renzo, J. De Rosny, M. Debbah, M. Alouini, and R. Zhang, “Wireless communications through reconfigurable intelligent surfaces,” *IEEE Access*, vol. 7, pp. 116 753–116 773, 2019.

[8] A. Guerra, F. Guidi, D. Dardari, A. Clemente, and R. D’Errico, “A millimeter-wave indoor backscattering channel model for environment mapping,” *IEEE Transactions on Antennas and Propagation*, vol. 65, no. 9, pp. 4935–4940, 2017.

[9] L. Di Palma, A. Clemente, L. Dussopt, R. Sauleau, P. Potier, and P. Pouliguen, “Circularly-polarized reconfigurable transmitarray in ka-band with beam scanning and polarization switching capabilities,” *IEEE Transactions on Antennas and Propagation*, vol. 65, no. 2, pp. 529–540, 2016.

[10] B. Akgun, M. Krunz, and D. Manzi, “Impact of beamforming on delay spread in wideband millimeter-wave systems,” in *2020 International Conference on Computing, Networking and Communications (ICNC)*. IEEE, 2020, pp. 890–896.

[11] A. Simonsson, H. Asplund, J. Medbo, and K. Werner, “Beamforming impact on time dispersion assessed on measured channels,” in *2018 IEEE 87th Vehicular Technology Conference (VTC Spring)*. IEEE, 2018, pp. 1–6.